ADVANCED MATERIALS
www.advmat.de

# Strain-Engineered Monolithic Multi-Band LEDs for Simultaneous Short-Wavelength and Mid-Wavelength Infrared Emission

*Hee Joon Jung, Dongwan Kim, Phuc Dinh Nguyen, Sangjun Kang, Jiyeon Jeon, Thu Trang Thi Bui, Jungwon Yoon, Minkyeong Kim, Changsug Lee, Robert Sinclair, In-Ho Lee,* Byong Sun Chun,* and Sang Jun Lee**

**Multiple quantum well (MQW) light-emitting diodes (LEDs) provide precise wavelength control, making them ideal light sources. However, achieving simultaneous short-wavelength infrared (SWIR, 1–3 µm) and mid-wavelength infrared (MWIR, 3–5 µm) emission from a single LED presents significant technical challenges due to lattice mismatch and reduced quantum efficiency when MQW structures with distinct bandgap energies are integrated onto a single substrate. As a result, most LEDs typically operate in only one IR band. In this study, monolithic multi-band MQW LEDs capable of simultaneous SWIR and MWIR emission are demonstrated. Strain engineering via Sb doping in the QWs induces well-distributed local lattice distortions, such as modulations of atomic bond angles and lengths, leading to balanced strain compensation and coherent epitaxy with atomically sharp interfaces within the MQWs. Reducing the QW thickness of InAsSb enhances quantum confinement, enabling simultaneous SWIR and MWIR emission at 2.87 and 3.18 µm. To further extend the emission range, a simulation-based fabrication feasibility map is developed, and an additional monolithic LED that emits simultaneously at 2.63 and 3.34 µm is fabricated. The monolithic integration of multi-band emission into a single device not only reduces size and complexity but also facilitates multispectral analysis for future optoelectronic devices.**

## 1. Introduction

Optoelectronic devices that integrate photodetectors with light-emitting diodes (LEDs) are widely utilized for applications based on absorption wavelengths.[1,2] Particulary, III-V compound semiconductor LEDs show promise due to their high quality and low defect density, which enhances light-emission efficiency through improved electron–hole recombination.[3–5] Infrared (IR) LEDs have garnered significant attention across a wide range of applications. Short-wavelength IR (SWIR, 1–3 µm) LEDs are used in non-invasive spectroscopy and biomedical imaging due to their ability to penetrate tissues and resolve molecular features. Mid-wavelength IR (MWIR, 3–5 µm) LEDs are valuable for industrial process control and environmental monitoring, as they exploit their strong interaction with molecular vibrations and thermal emissions.

Multiple quantum well (MQW) LEDs offer precise wavelength control through

H. J. Jung, D. Kim, P. D. Nguyen, J. Jeon, T. T. T. Bui, I.-H. Lee, B. S. Chun, S. J. Lee
Korea Research Institute of Standards and Science
Daejeon 34113, Republic of Korea
E-mail: ihlee@kriss.re.kr; mainue@kriss.re.kr; sjlee@kriss.re.kr

P. D. Nguyen, T. T. T. Bui, B. S. Chun, S. J. Lee
Department of Nano Science
University of Science & Technology
Daejeon 34113, Republic of Korea

The ORCID identification number(s) for the author(s) of this article can be found under https://doi.org/10.1002/adma.202508332



**DOI: 10.1002/adma.202508332**

S. Kang
In-situ Electron Microscopy
Department of Materials Science
Technical University of Darmstadt
64287 Darmstadt, Germany

J. Yoon, M. Kim, C. Lee
R&D Center IRSpectra Co., LTD
Daejeon 34113, Republic of Korea

R. Sinclair
Department of Materials Science and Engineering
Stanford University
Stanford, CA 94305, USA

S. Kang
Institute of Nanotechnology
Karlsruhe Institute of Technology
76344 Eggenstein-Leopoldshafen, Germany

 

adjustments to the thickness and composition of quantum wells (QWs) and quantum barriers (QBs), making them suitable for multispectral light sources.[6–8] In the visible light band, multispectral LEDs have been developed by constructing tandem devices,[9] stacking red/green/blue LEDs,[10] or using MQWs with varied lattice constants.[11–13] In the MWIR band, multispectral MQWs have been realized by stacking InSb MQWs and AlInSb layers on a GaSb/GaAs interface misfit array.[14] Despite these advances, devices typically emit light in a single IR band.

This limitation arises primarily because simultaneous SWIR and MWIR emission requires the integration of semiconductor materials with different bandgap energies, leading to lattice mismatch and defect formation when both materials are grown on a single substrate. Such mismatches reduce quantum efficiency and increase interlayer stress, which can cause epitaxial-layer cracking, disrupt the MQW energy band structure, and limit electron–hole recombination.[15–18] Consequently, developing an LED capable of simultaneous emission in both the SWIR and MWIR bands remains a challenge. Existing approaches typically rely on separate devices for each band, which can introduce boresight misalignment and temporal desynchronization. This significantly limits the ability to acquire synchronized multi-band information, thereby reducing the versatility and functionality of IR LEDs. Monolithic multi-band LEDs are therefore essential, as a single device capable of simultaneous SWIR and MWIR emission improves system compactness, reduces cost, and enables more versatile and efficient IR sensing and imaging applications. To the best of our knowledge, no monolithic multi-band LED emitting simultaneously in both IR bands has been reported, highlighting the crucial need for such devices.

In this study, we demonstrate monolithic multi-band MQW LEDs capable of simultaneous SWIR and MWIR emission using InAsSb, a material typically applied for MWIR emission. By incorporating InAsSb QWs, InAsPSb QBs, and metamorphic buffer layers and applying strain engineering, we achieved high-quality MQWs with atomically sharp interfaces and coherent epitaxy. This design overcomes the crystallographic and electrical challenges associated with differing bandgaps, allowing for simultaneous emission at 2.87 µm (SWIR) and 3.18 µm (MWIR) with output powers of 14 and 30 µW, respectively. Simulations indicate that reducing the QW thickness enhances quantum confinement effects, facilitating shorter-wavelength photon emission. To design LEDs with a broad emission range across the SWIR and MWIR bands, we developed a simulation-based fabrication feasibility map that incorporates both the peak emission wavelength and low strain energy, with parameters determined by the QW thickness and Sb composition. Consequently, we successfully fabricated another monolithic MQW LED capable of simultaneous emission at IR wavelengths of 2.63 and 3.34 µm. The fabricated monolithic multi-band MQW LEDs demonstrate stable, simultaneous SWIR and MWIR emission with precise strain compensation, enhanced quantum confinement, and high structural quality, offering a practical platform for compact, tunable, and efficient IR optoelectronic devices.

## 2. Results and Discussion

### 2.1. Fabrication and Crystallographic Analysis of Monolithic Multi-Band LEDs

Before developing monolithic multi-band LEDs, we fabricated single SWIR and MWIR MQW LEDs. In QWs, electrons are confined as quantized waves. A reduction in QW thickness strengthens the confinement, thereby increasing the energy separation between the quantized states. This results in an increased electron–hole energy gap, which leads to shorter-wavelength photon emission. We simulated the potential of InAsSb, a material typically used for MWIR emission, for SWIR emission using the commercial Nextnano++ package.

**Figure 1a** shows that as the InAsSb QW thickness decreases from 12 to 4 nm, the simulated emission wavelength decreases from 3.25 µm (MWIR) to 2.85 µm (SWIR). Based on these simulations, we fabricated single SWIR and MWIR LEDs and measured their electroluminescence (EL). The experimental results closely matched the simulation results regarding the QW thickness (Figure 1b). We selected QW/QB thicknesses of 4/18 nm and 12/24 nm for the SWIR and MWIR MQW LEDs, respectively.

Figure 1c,d shows the high-resolution X-ray diffraction (HRXRD) $\omega$-$2\theta$ rocking curves near the (004) symmetric reflection, where diffraction intensity is maximized due to the large scattering factor, and the reciprocal space map (RSM) near the (115) asymmetric reflection, chosen for its high sensitivity to strain in the material, for both single LEDs. Herein, the RSM was obtained by varying the reflection angles within a given range to map the diffraction peaks of the sample using the X'Pert MRD HRXRD system and X'Pert epitaxy software. The reciprocal lattice points were subsequently extracted from the diffraction pattern based on the peak positions, and the calculations were performed using the same system and software. The experimental results align well with theoretical simulation results, indicating a high degree of structural homogeneity. The $\omega$-$2\theta$ peaks (Figure 1c) and reciprocal lattice points (RLPs, Figure 1d) clearly identify the InP substrate, InAsPSb cladding layer, and InAsP metamorphic buffer layer. From the measurement of the $\omega$-$2\theta$ rocking curves and reciprocal lattice coordinates, we calculated the InAsP metamorphic buffer lattice constants as $a_{\perp}$ ≈6.03 Å (out-of-plane) and $a_{\parallel}$ ≈6.03 Å (in-plane), indicating near-complete strain relaxation of ≈99.9% (Experimental Section and Note S2, Supporting Information). Clear MQW satellite peaks were observed for both MWIR and SWIR channels, signifying a homogeneous periodic structure and well-defined MQW interfaces. Our MQWs are designed to be strain-compensated with accumulated strain energy below the dislocation-formation threshold.[19] Consequently, the fully strained MQWs exhibit satellite peaks with the same $Q_{[110]}$ reciprocal lattice coordinate as the InAsP metamorphic buffer, corresponding to the same in-plane lattice constant.

Furthermore, the MQW satellite peaks were preserved for the monolithic multi-band LED, demonstrating no degradation of epitaxial quality during integration (Figure 1e,f). Figure 1g,h presents a top view and schematic diagram of the fabricated monolithic multi-band LEDs, respectively. Details regarding the InAsP metamorphic buffers, MQW growth, and fabrication of

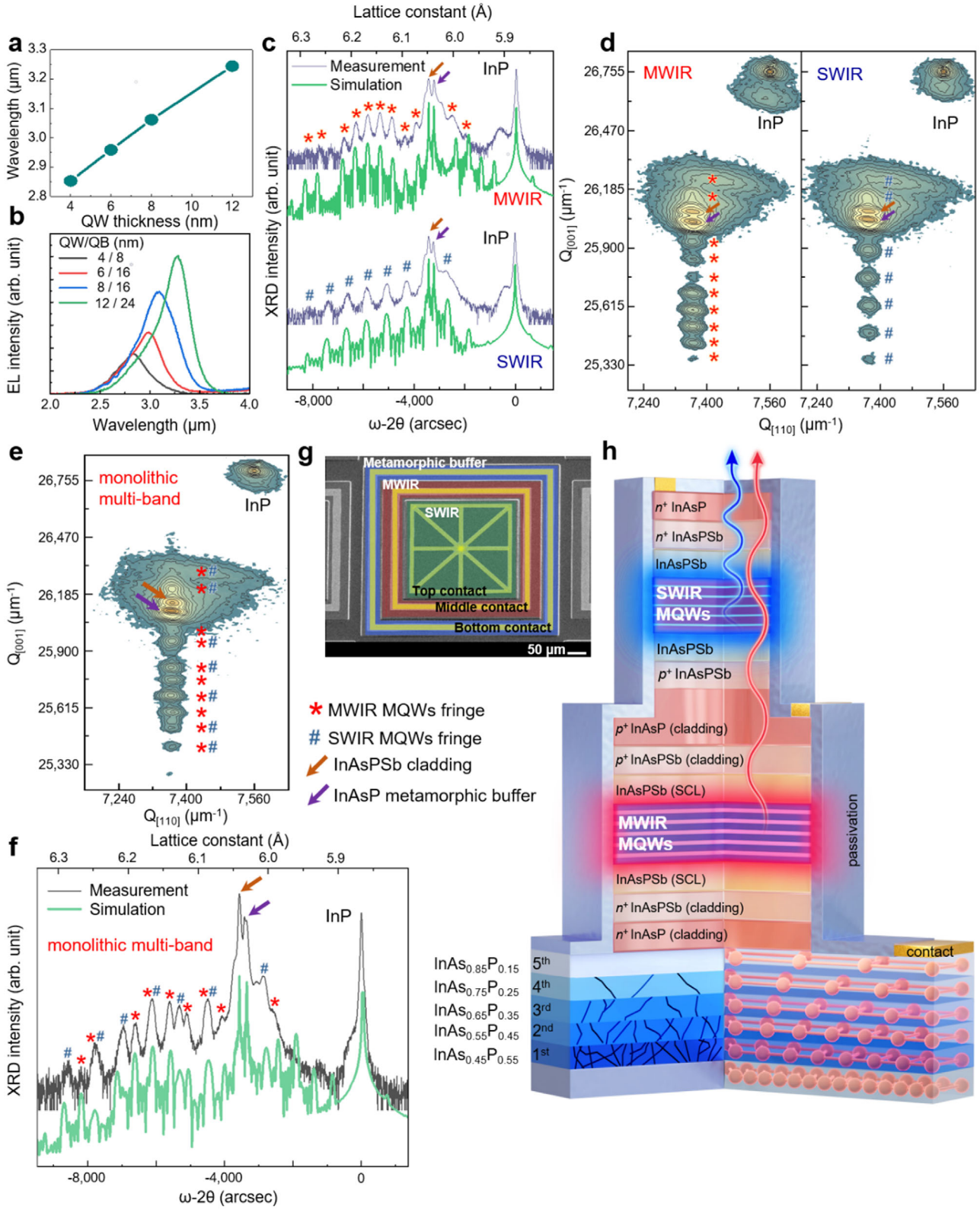


**Figure 1.** Fabrication and characterization of single SWIR and MWIR MQW LEDs and monolithic multi-band MQW LEDs. a) Simulated emission wavelength as a function of the InAsSb QWs thickness. b) EL spectra of the fabricated single SWIR and MWIR MQW LEDs. c) HRXRD $\omega$-$2\theta$ rocking curves and d) RSMs for the single SWIR and MWIR MQW LEDs. e) RSMs and f) HRXRD $\omega$-$2\theta$ rocking curves for the monolithic multi-band MQW LEDs. g) Top view of the fabricated monolithic multi-band MQW LEDs. h) Schematic diagram of the monolithic multi-band LEDs.

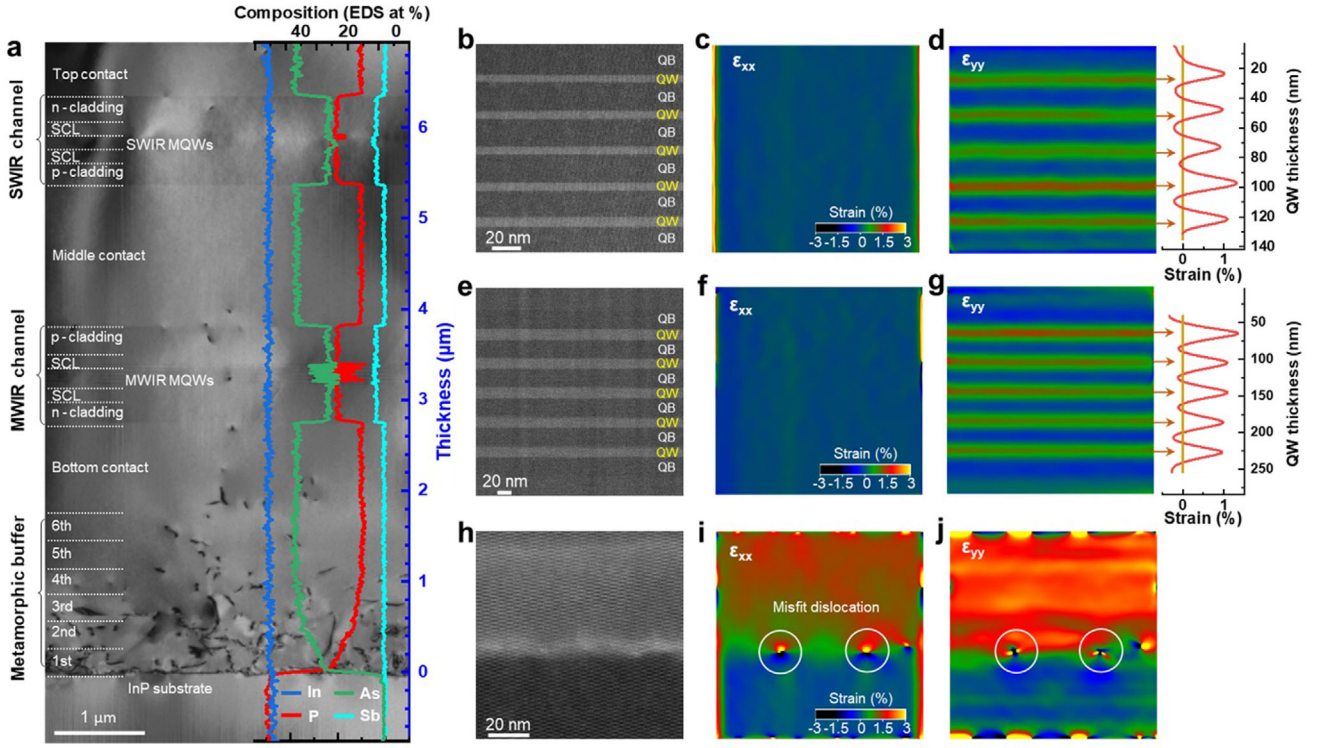


**Figure 2.** Dislocation distribution in monolithic multi-band LED and coherent lattice matching in MQWs/MQBs. a) Cross-sectional BFTEM image of a tandem structure comprising SWIR (top), MWIR (middle), and a metamorphic buffer (bottom), overlaid with an EDS elemental profile showing the distribution of In, As, P, and Sb. b–j) Sets of AC-HAADF-STEM images with GPA-assisted horizontal strain ($\varepsilon_{xx}$) and vertical strain ($\varepsilon_{yy}$) fields from the (b–d) top SWIR, (e–g) middle MWIR, and (h–j) bottom metamorphic buffer on the InP substrate. (c,d,f,g,i,j) Strain fields contours every 0.2% ranging from −3% to +3%. The averaged vertical strain ($\varepsilon_{yy}$) line profiles for (d) SWIR and (g) MWIR MQWs/MQBs are shown alongside. Note that the coherent epitaxy of MQWs/MQBs exhibits negligible horizontal strain, while the interface between the metamorphic buffer and InP substrate shows significant strain with misfit dislocations.

monolithic multi-band LEDs are presented in the Experimental Section.

The dislocation distribution was examined using bright-field transmission electron microscopy (BFTEM) (**Figure 2a**).[20] During the growth of the InAsP metamorphic step buffer, the strain caused by lattice mismatch was alleviated through the generation of misfit dislocations. Most dislocations are predominantly confined within the first step buffer due to the substantial lattice mismatch between the $InAs_{0.45}P_{0.55}$ layer and the InP substrate. As growth progresses, misfit dislocations glide upward along {111} half-planes in the <110> direction as threading dislocations.[21] These dislocations terminate or interlock,[22] reducing the dislocation density from the 2nd to 5th step buffer. Notably, threading dislocations are scarce in MWIR and SWIR MQWs.

The aberration-corrected high-angle annular dark-field scanning transmission electron microscopy (AC-HAADF-STEM) images in Figure 2h and Figure S6 (Supporting Information), along with the geometric phase analysis (GPA) results in Figure 2i,j,[23] reveal strongly strained regions around two misfit dislocation cores (≈30 nm apart) at the InP substrate/InAsP first step buffer interface. The high initial dislocation density increases the probability of interaction and annihilation. Although a high activation energy is required for annihilation, the structure can relax more effectively once strain release is initiated in the high-density regions.[24] Additionally, using an anion-mixed InAsP buffer, rather than a cation-mixed InAlAs buffer, proved advantageous due to the equivalent formation energies of orthogonal edge and screw dislocations (i.e., 1/2[110]{111} and 1/2[1$\bar{1}$0]{111}), which led to increased relaxation and reduced lattice tilting.[25]

### 2.2. Coherent Lattice Matching and Strain Compensation in QWs and QBs

The AC-HAADF images of the MQWs in the SWIR and MWIR channels, with drift-corrected frame integration (DCFI), are shown in Figure 2b,e, Figures S6, and S7 (Supporting Information). These images reveal atomically sharp interfaces between the InAsSb QWs and InAsPSb QBs across a surveyed area of ≈2 µm, indicating the effective suppression of discrete 3D island growth. The enthalpy of formation of In—Sb (−36.9 ± 0.6 kJ $mol^{-1}$) is lower than that of In—As (−62.8 ± 1.0 kJ $mol^{-1}$) and In—P (−74.0 ± 4.4 kJ $mol^{-1}$) at 500 °C.[26] This causes Sb to dissociate from In atoms at the surface, where it segregates and modifies the surface energy or growth kinetics, behaving like a surfactant (Note S3, Supporting Information). This segregation reduces the surface diffusion length of other adatoms and promotes 2D layer-by-layer growth.[27] The InAsSb QW/InAsPSb QB interfaces are free of stacking faults, demonstrating the effectiveness of the strain compensation design.

To unveil the strain distribution in the MQW/MQB, GPA (Figure 2c,d,f,g) was performed on each HAADF-STEM image,[23] revealing variation in the average vertical strain ($\varepsilon_{yy}$) along the growth direction, as shown next to Figure 2d,g. The mean (standard deviation) of the horizontal strain ($\varepsilon_{xx}$) for the SWIR (Figure 2c) and MWIR MQWs (Figure 2f) is +1.7 × $10^{-3}$% (±3.5 × $10^{-2}$%) and −4.8 × $10^{-4}$% (±4.3 × $10^{-2}$%), respectively, confirming coherent epitaxy with excellent lateral lattice matching (i.e., stress-free). These values are statistically derived from ≈$10^7$ data points across 5 × $10^4$ $nm^2$. The negligible lateral strain indicates effective compensation of the vertical compressive stress in $InAs_{0.9}Sb_{0.1}$ QWs ($a$ = 6.088 Å) and tensile stress in $InAs_{0.3}P_{0.65}Sb_{0.05}$ QBs ($a$ = 6.003 Å), despite a lattice-parameter difference of ≈1.4% (Experimental Section and Note S2). Thus, the lateral strain is relieved in the out-of-plane direction. Consequently, $\varepsilon_{yy}$ in both channels shows that the significant tensile strain of +1.05% (±0.14%) and 1.09% (±0.14%) in the InAsSb QWs is balanced by a counteracting compressive strain of −0.17% (±0.05%) and −0.14% (±0.06%) in the InAsPSb QBs for SWIR and MWIR, respectively. This trend was confirmed by vertical streaking of 00l reflections, contrary to spherical hk0 spots from selected area diffraction (SAD) in Figure S10 (Supporting Information) for both SWIR and MWIR MQWs/MQBs.

Further strain analysis was performed using cepstral 4D STEM by leveraging the exit-wave power-cepstrum transform (EWPC) applied to a processed 4D nano-beam diffraction dataset (Note S9, Supporting Information).[28] The cepstral 4D STEM in Figure S18 (Supporting Information) reconfirms identical strain trends ($\varepsilon_{xx}$ and $\varepsilon_{yy}$) in the MWIR MQWs/MQBs. Both strain maps illustrate that the horizontal inner stress is well balanced, even though the materials of QW and QB are different.

### 2.3. Atomic-Scale Local Lattice Distortions and Coherency

The strain relaxation at the atomic scale, demonstrating excellent coherent integration across our QW/QB structures, was examined. In **Figure 3a**, 10% Sb-doped InAs bonds (referred to as "dumbbells") in a SWIR QW are frequently oriented to the left and right due to local lattice distortions, as indicated by red and blue arrows, respectively, while green arrows indicate undistorted dumbbells. The average contrast profile (Figure 3b) shows the roughness of 1–2 (002) layers over the QW and QB interfaces. The dumbbell tilting (Figure 3c) and columnar elongation (Figure 3d) result from a minuscule shift (less than a few tens of picometers) in entire or partial atomic columns, which provides flexible strain relief and prevents strain accumulation that could lead to misfit dislocations. Moreover, localized deformations can result in altered positional distributions of some atoms, leading to misalignment of atomic columns in the projection view.

To confirm the misalignment effect on the [110] projection, a supercell was created in Figure 3e with 50% of the In atoms identically shifted by 13.6 pm due to 25% Sb substitutional atoms in an As column. The corresponding HAADF images were obtained via multi-slice simulations using Dr. Probe,[23] as shown in Figure 3e and Figures S8, S9, S14, and S15 (Supporting Information), and reveal a slight dumbbell tilting and contrast elongation of the In column with off-centered In atoms next to Sb substitutional atoms (Note S8, Supporting Information). The observed local distortions, such as dumbbell tilting and contrast elongation, are associated with shifts of partial atoms in each column.[29] Similar phenomena have been observed in multiferroic oxides,[30] perovskites,[31] thermoelectric materials,[32,33] and ferroelectric materials.[34] These local distortions at the atomic level are properly dispersed to balance the lateral lattice mismatch across the QW/QB interfaces, resulting in overall coherent growth with strain relaxation.

To clarify the effect of Sb incorporation into the InAs crystal structure at the atomic level, we utilized artificial neural network (ANN)-based potentials.[35] These ANN-generated supercells are reconstructed along [110] projection using Dr. Probe to see the misalignment effect on HAADF with the randomly positioned atoms (Figures S11–S13, Supporting Information). The cropped supercell (12 nm thick) and corresponding HAADF simulation (probe FWHM of 40 pm) in Figure 3f exhibit clear columnar elongation. Even when considering only the front two (110) layers out of the 12 nm-thick supercell in Figure 3g, the localized deformations by Sb substitution trigger significant variation in adjacent bonding lengths (2.70–2.85 Å) and angles (107.25–112.95°).

The ANN calculations over 1000 supercells revealed that Sb doping statistically alters bond lengths and angles with 1.7% volumetric expansion of the crystal compared to undoped structures, as illustrated in Figure 3h,i (more details in Experimental Section). The average In—As bond lengths tend to be slightly longer, though they can also be shorter in some cases, while the In—Sb bonds lengthen by 4–5%, leading to an off-centered displacement of 11–13 pm. The In—As—In bond angles were found to increase by ≈0.5° on average, with some cases showing variations of up to ±1° in either direction. In the distribution of In—Sb—In bond angles, the most frequent deviation from the reference value (109.5°) is a decrease of ≈1°, followed by an increase of 1° as the second most frequent deviation. Thus, the ANN-based findings agree with the empirical atomic configuration, emphasizing the significant effect of Sb doping on the atomic-scale arrangement with regard to strain relaxation and coherent growth of the QW.

### 2.4. Simultaneous SWIR and MWIR Emission from Monolithic Multi-Band MQW LEDs

We fabricated monolithic multi-band MQW LEDs. The emission EL spectrum was measured by simultaneously biasing the LEDs (Figure 1g,h). The components of the spectrum were separated through Gaussian fitting. The changes observed in the second-order derivative of the EL intensity at 2.87 and 3.18 µm in **Figure 4a** indicate that both SWIR and MWIR emissions occur simultaneously at room temperature.

The primary difference between the LEDs lies in the QW/QB thickness: 4/18 nm for SWIR and 12/24 nm for MWIR. Under fully relaxed strain conditions, quantum confinement effects significantly influence the electronic properties of the QWs—particularly as their thickness decreases. In thinner quantum wells, stronger quantum confinement leads to an increased energy separation between the quantized electron and hole states. Consequently, thinner QWs exhibit a larger bandgap, resulting in shorter-wavelength photon emission. The simulated energy

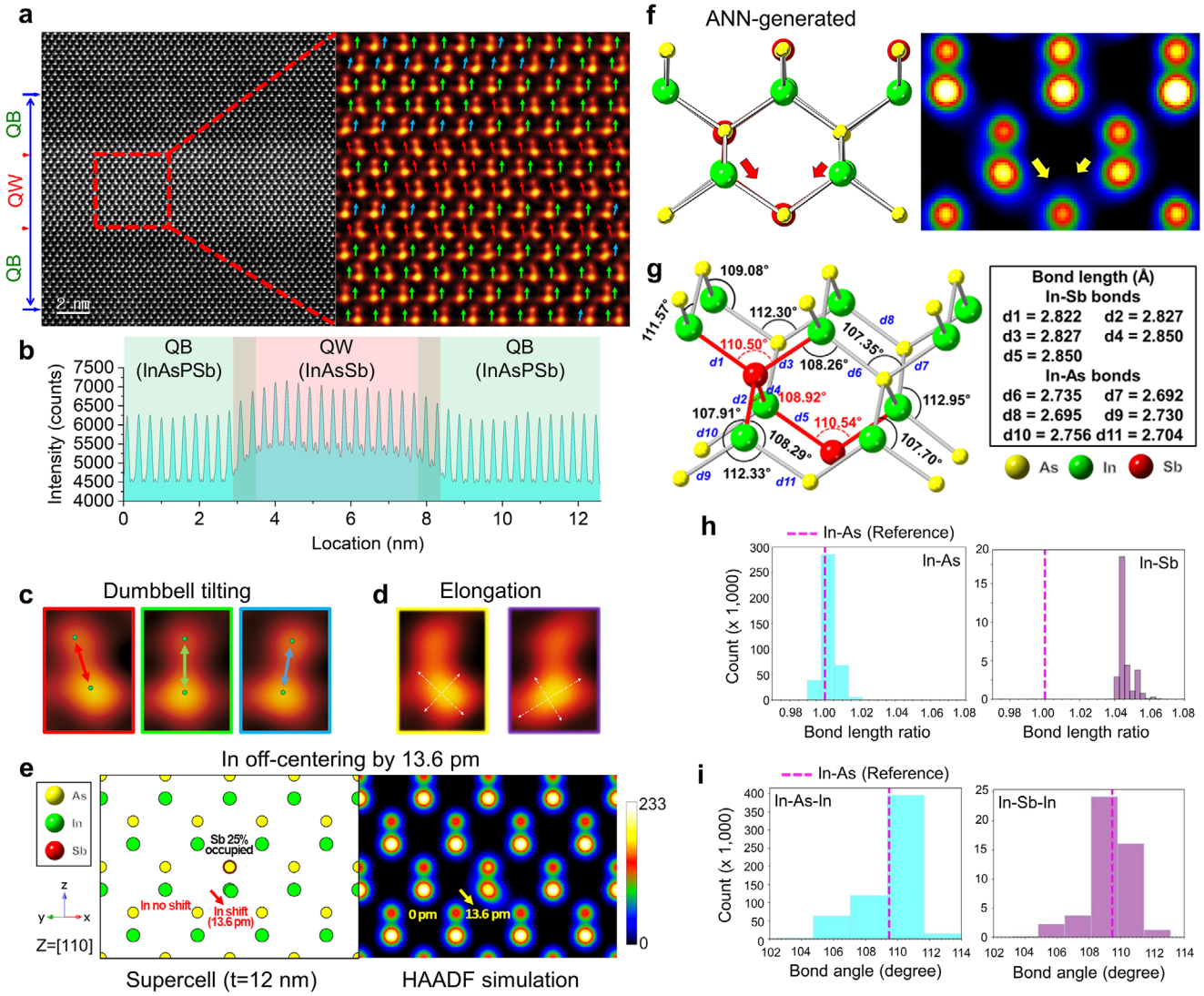


**Figure 3.** Scattered lattice distortion and strain compensation due to Sb substitution. a) Atomic HAADF image of a SWIR QW (left) and the distribution of color-coded dumbbell tilting within the QW from the red box (right). b) Contrast line profile over the QW. c) Enlarged dumbbells exhibit tilting to the left (red), right (blue), and others are undistorted (green). d) Elongated contrast due to misaligned atoms from the original axial coordinates. e) Simulated contrast elongation from an In column associated with substitutional Sb atoms (25%) in an As column. f) Misaligned In atoms projection due to adjacent Sb atoms and the corresponding HAADF simulation: The [110]-projected segment (12 nm thick) was created from an ANN-generated supercell with 108 In, 100 As, and 8 randomly located Sb atoms (more details in Note S8, Supporting Information). g) A molecular structure of only two front (110) stacking from (f), showing the local distortion of bond lengths and angles due to Sb substitution. h,i) Statistical distribution of bond lengths and bond angles from 1000 supercells (Sb atom-doped InAs supercells composed of 108 In, 100 As, and 8 Sb atoms).

band profiles for both SWIR and MWIR reveal a split between heavy- and light-hole energy levels of $\Delta E_{VB} = 64$ meV within the valence band due to the strain in the QWs (Figure 4b). HAADF-STEM-GPA results indicate that some strain remains, although it has been significantly mitigated for coherent growth. Notably, in the SWIR case only, the conduction-band electron wave function extends partially into the neighboring QBs (Figure 4b) due to strong quantum confinement. The relationship between energy and QW width is governed by quantum confinement effects, where the quantum energy is inversely proportional to the square of the QW width, which is typical of quantum confinement (Figure 4c).

Thus, despite minimal strain, the dominant quantum confinement effect arising from the thickness difference facilitates simultaneous SWIR and MWIR emission. Furthermore, the optical transition energies ($E_1 - HH_1$) for SWIR and MWIR are calculated to be 439 meV (2.82 μm) and 391 meV (3.17 μm), respectively (Figure 4b), which agrees with the experimental data (Figure 4a). With quasi-continuous-wave current injection of 250 mA, our monolithic LEDs achieved optical powers of 14 and 30 μW for SWIR and MWIR emission, respectively (Figure 4d).

The temperature dependence of the EL intensity is presented in Figure 4e, where emissions from the SWIR channel (blue area) and MWIR channel (red area) are identified. Within the

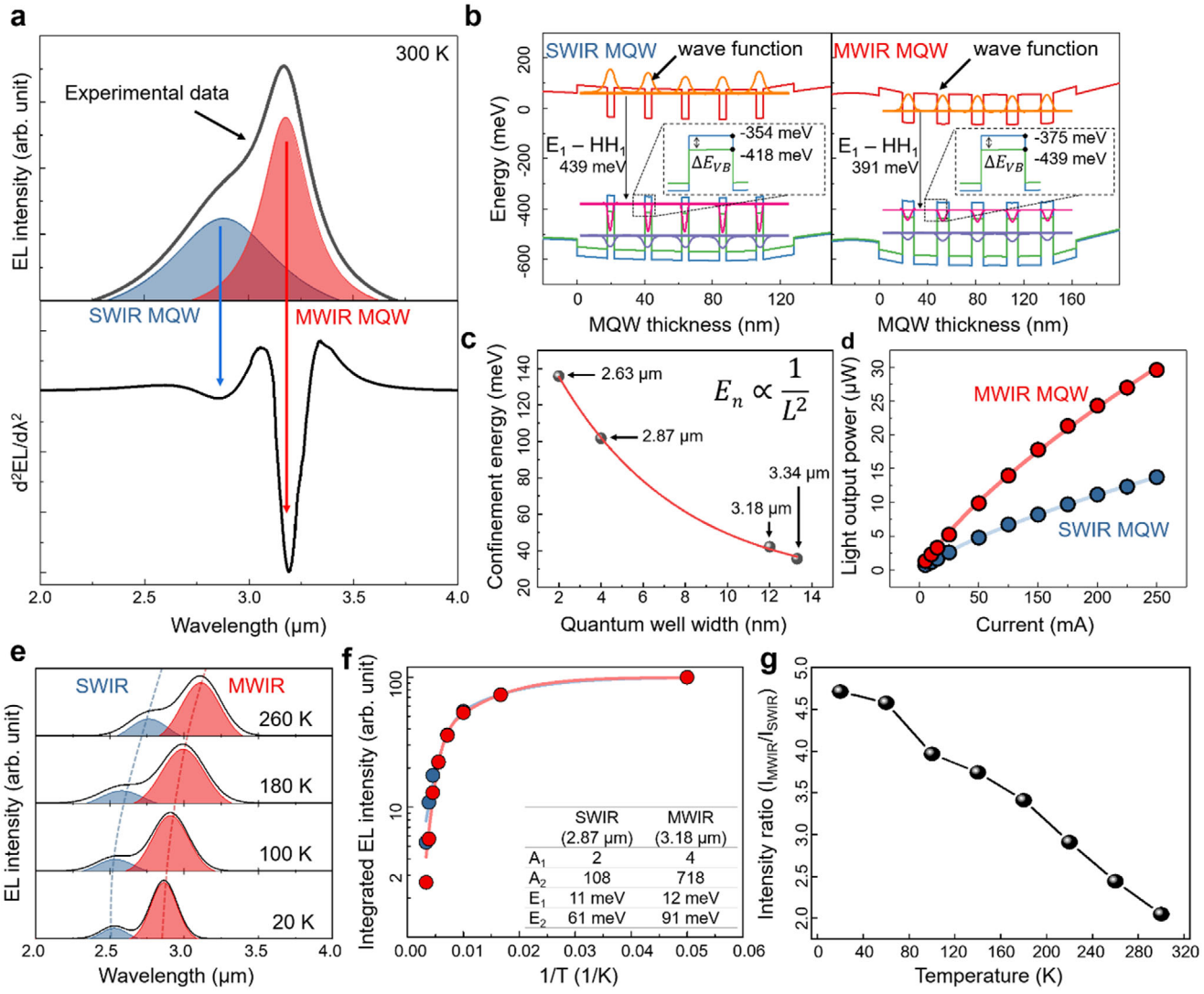


**Figure 4.** Characterization of monolithic multi-band MQW LEDs. a) EL spectrum of the monolithic multi-band MQW LED measured under simultaneous biasing of the SWIR and MWIR LEDs. The second-order derivative of the EL intensity reveals distinct emission peaks at 2.87 μm (SWIR) and 3.18 μm (MWIR). b) Simulated energy band profiles for SWIR and MWIR MQWs, showing electron wave function overflows into neighboring QBs in the SWIR QWs. c) Relationship between energy and QW width. d) Optical power output of the monolithic multi-band MQW LEDs under quasi-CW current injection. e) Temperature-dependent EL intensity of the monolithic multi-band MQW LEDs. f) Arrhenius model fitting for analyzing non-radiative recombination. g) EL intensity dependence on temperature.

temperature range of 20–180 K, the SWIR and MWIR emissions are clearly distinguishable. However, between 220 and 300 K, the EL intensity of both channels decreases due to the non-radiative recombination. To analyze the non-radiative recombination mechanism in our multi-band MQWs LED, the EL intensity data were modeled using a second-order Arrhenius equation (Figure 4f).[36]

$$I(T) = \frac{I_0}{1 + A_1 \exp\left(-\frac{E_1}{k_B T}\right) + A_2 \exp\left(-\frac{E_2}{k_B T}\right)} \quad (1)$$

where $I_0$ is the EL intensity at 0 K, $A_1$ and $A_2$ denote the rate constant related to non-radiative recombination, $E_1$ and $E_2$ represent the activation energies for non-radiative recombination at low and high temperatures, respectively. $T$ is the temperature and $k_B$ is the Boltzmann constant. The activation energies $E_1$ for SWIR and MWIR MQWs are 11 and 12 meV, respectively, corresponding to the thermal activation energy required to excite a weakly localized carrier within the QW.

The activation energies $E_2$ for carrier escape from the QW to the QB are 61 and 91 meV for SWIR and MWIR MQWs, respectively. This indicates that the SWIR MQWs have a lower activation energy for carrier escape into non-radiative recombination pathways at higher temperatures compared to MWIR MQWs. This observation aligns with simulation results, which show that strong quantum confinement in SWIR MQWs causes the electron wave function to extend beyond the thin QW region,

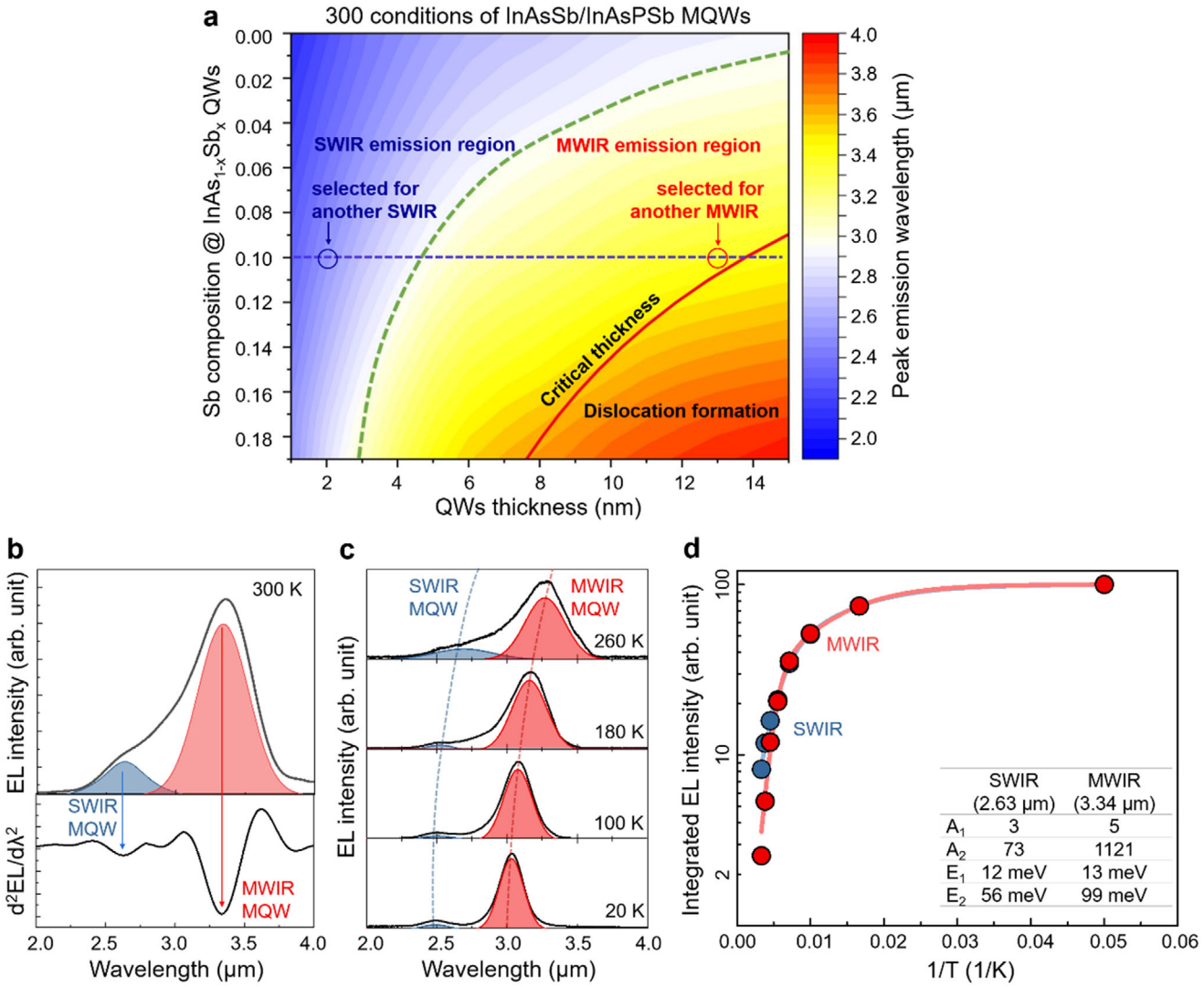


**Figure 5.** Optimization and extension of multi-band emission in monolithic MQW LEDs. a) Simulation-based fabrication feasibility map for designing monolithic multi-band MQW LEDs by controlling QW thickness and Sb composition. b) Fabrication of another monolithic multi-band LED using the feasibility map, with QW/QB thickness of 2/19 nm for 2.63 μm emission and 13/26 nm for 3.34 μm emission, with fixed Sb composition of 10%. c) Temperature-dependent EL intensity of the fabricated monolithic multi-band MQW LEDs. d) Arrhenius model fitting for analyzing non-radiative recombination.

allowing some electron density to occupy the QB. Consequently, SWIR MQWs exhibit a lower activation energy for electron escape to non-radiative recombination.

However, the decrease in EL intensity with increasing temperature is more pronounced in MWIR MQWs than in SWIR MQWs due to a higher value of $A_2$ (Figure 4g). In narrow bandgap materials, the energy released during carrier recombination is often insufficient to overcome the phonon energy threshold, making it more likely to be absorbed by phonons rather than emitted as photons. This higher phonon absorption in MWIR MQWs leads to a more significant reduction in EL intensity with increasing temperature, despite the higher activation energy for non-radiative recombination.

To extend the emission range across both SWIR and MWIR bands, we developed and utilized a fabrication feasibility map that enables the design of a monolithic multi-band LED capable of simultaneous emission across a wider range of infrared wavelengths (**Figure 5a**). This map, developed through simulations, integrates key factors such as dislocation density and strain energy by adjusting the QW thickness and Sb composition (Experimental Section and Note S6, Supporting Information).

By applying the feasibility map, we successfully fabricated an additional monolithic LED that simultaneously emits at 2.63 and 3.34 μm, with QW/QB thicknesses of 2/19 and 13/26 nm for SWIR and MWIR emission (Figure 5b). This achievement demonstrates the remarkable versatility and precision of our approach, resulting in a robust multi-band LED that extends the emission range beyond previous limits. The feasibility map not only facilitated an efficient design for dual-band emission, but also enabled the extension of the emission spectrum, greatly

enhancing the practical applicability of multi-band LEDs across a wider SWIR and MWIR range.

## 3. Conclusion

We developed monolithic multi-band MQW LEDs capable of simultaneous SWIR and MWIR emission, representing a notable advancement in optoelectronic technology. Our monolithic multi-band MQW LEDs, with QW/QB thicknesses of 4/18 (2/19) and 12/24 (13/26) nm, emitted light at wavelengths of 2.87 (2.63) and 3.18 (3.34) µm. Strain-compensated designs incorporating InAsSb QWs and InAsPSb QBs were validated via HRXRD and reciprocal space mapping, confirming excellent structural homogeneity and near-complete relaxation (99.9%) in the InAsP metamorphic buffer. Clear MQW satellite peaks and balanced tensile and compressive strains across QWs and QBs indicated effective strain compensation. AC-HAADF-STEM imaging verified atomically sharp QW/QB interfaces without stacking faults and revealed localized lattice distortions that facilitated strain relaxation. Additionally, ANN-based potential calculations revealed modifications in bond lengths and angles due to Sb incorporation, which enhanced strain relaxation. These results highlight the structural integrity and effective strain management of our monolithic MQW LEDs, which enable high-performance, simultaneous multi-band IR emission.

## 4. Experimental Section

*Growth and Fabrication of Monolithic Multi-Band MQWs LED using InAsP Metamorphic Buffer Layers*: Samples were grown in a Veeco D180 low pressure metal–organic chemical vapor deposition (LP-MOCVD) system. Trimethylindium ($In(CH_3)_3$), trimethylantimony ($Sb(CH_3)_3$), arsine ($AsH_3$), and phosphine ($PH_3$) were used as precursors. Diethylzinc ($Zn(C_2H_5)_2$) and hydrogen-diluted silane ($SiH_4$:$H_2$) were used as p-type and n-type dopants, respectively. The growth pressure was 1 bar under pure $H_2$ flow, and the growth temperature was set at 540 °C. Epi-ready semi-insulating InP (001) substrates (AXT) were used for the growth of multi-band InAsSb/InAsPSb MQWs LEDs.

Due to the very thin thickness of the QWs and QBs, accurate determination of lattice parameters using HR-XRD becomes challenging. However, by inputting the expected compositions used to grow the QWs and QBs into the X'Pert epitaxy software and iteratively comparing the simulated diffraction curves with the experimental data, the composition that best matches the curves can be identified. Based on this composition, the lattice parameters can then be determined using the data library of the X'Pert epitaxy software. Using this approach, the lattice parameters of the $InAs_{0.9}Sb_{0.1}$ QWs and $InAs_{0.3}P_{0.65}Sb_{0.05}$ QBs were obtained as 6.088 and 6.003 Å, respectively.

To address the significant lattice mismatch between the InP substrate ($a$ = 5.869 Å) and the MQWs, a metamorphic buffer growth technique was employed, involving a gradual increase in the As composition within the n-type $InAs_yP_{1-y}$ layer. Six successive 300 nm-thick n-type $InAs_yP_{1-y}$ layers were deposited on the InP substrate as metamorphic buffer layers. To minimize the generation of threading dislocations, the first metamorphic layer was grown with $InAs_{0.45}P_{0.55}$ ($a$ = 5.978 Å), resulting in a ≈1.9% lattice mismatch with the InP substrate. In subsequent layers, from the second to the fifth, the lattice constant increases with the As composition in $InAs_{0.55}P_{0.45}$ ($a$ = 5.978 Å), $InAs_{0.65}P_{0.35}$ ($a$ = 5.988 Å), $InAs_{0.75}P_{0.25}$ ($a$ = 5.998 Å), and $InAs_{0.85}P_{0.15}$ ($a$ = 6.039 Å), with the lattice parameter calculated using Vegard's law. The calculated lattice parameter of the top-most metamorphic buffer layer of $InAs_{0.85}P_{0.15}$ closely matches the experimental value of $a_{\perp,\parallel} \approx 6.03$ Å from the $\omega$-$2\theta$ rocking curves and RSM. The sixth layer, an overshoot layer of $InAs_{0.88}P_{0.12}$ ($a$ = 6.046 Å), provided the elastic energy required for full strain relaxation.

The multi-band InAsSb/InAsPSb MQW LEDs were monolithically grown on an InP substrate and consisted of two back-to-back connected MWIR and SWIR LED channels in the $n$/MWIR MQWs (bottom)/$p$/SWIR MQWs (top)/$n$ configuration. Each MQW consists of five $InAs_{0.9}Sb_{0.1}$/$InAs_{0.3}P_{0.65}Sb_{0.05}$ strain compensated MQWs. The QW/QB thicknesses were 12 nm/24 nm (13 nm/26 nm) and 4 nm/18 nm (2 nm/19 nm) for MWIR and SWIR channels, respectively. These MQWs were sandwiched between 100 nm $InAs_{0.54}P_{0.36}Sb_{0.1}$ separate confinement layer (SCL) and 400 nm $p^+/n^+$ $InAs_{0.3}P_{0.65}Sb_{0.05}$ cladding layer. Monolithic multi-band LEDs were fabricated using conventional photolithography and lift-off techniques. For each LED, a double mesa structure was used for multi-band emission (MWIR mesa size 420 × 420 µm² and SWIR mesa size 300 × 300 µm²). To avoid unwanted surface effects, the structure was passivated with 500 nm of $SiO_2$ using electron beam evaporation.

*EL and XRD Measurements*: For EL measurements, the LED chip was mounted in a copper package (LCC or TO8). The chip-package assembly was mounted on a helium-cooled cryostation equipped with a $Br_2$ window for infrared transmission. The emission signal was analyzed using a Horiba iHR-350 spectrometer and a nitrogen cooled InSb detector. To analyze the structural properties of the multi-band MQWs, samples were investigated using a Malvern Panalytical high-resolution X-ray diffractometer, equipped with Cu$K\alpha_1$ X-ray source ($\lambda$ = 1.5406 Å), hybrid 2 bounce Ge (220) monochromator. The lattice constant, strain, and crystal orientation were determined from the results analysis using X'Pert epitaxy software.

*TEM (AC-HAADF-STEM, BFTEM, GPA, Atomap, Cepstral 4D STEM, SAD)*: Cross-sectional TEM samples were prepared using a focused ion beam (FIB, FEI Helios NanoLab 650) at 30 kV using a Ga focused ion beam, and the sample surface was fine-cleaned using low acceleration of a 1 kV beam. An aberration-corrected/mono-chromated STEM (Spectra 300 X-FEG/Mono, Thermo Fisher Scientific) operated at 300 kV for EDS mapping using quadrant EDS detectors (Super-X SDD, Thermo Fisher Scientific) on the Spectra 300. The convergence angle and beam current for STEM-HAADF were 30 mrad (50 µm condenser aperture) and 65 pA, while those for EDS maps were 21.4 mrad (30 µm condenser aperture) and 250 pA. The collection angle of the HAADF was 65–200 mrad with a pixel dwell time of 10–15 µs and an area of 2048 × 2048 pixels. A multi-slice HAADF simulation was performed using Dr. Probe software, and the details of the simulation can be found in Figures S8 and S9 (Supporting Information). Analyses on lattice strain ($\varepsilon_{xx}$, $\varepsilon_{yy}$) and local distortion (dumbbell tilting), were supported by GPA code in DigitalMicrograph and Atomap software (python-based) with 2D Gaussian fitting, respectively.

The BFTEM (Figure 2a) was taken at weak beam diffraction conditions (tilted 5–6 degrees from the [110] zone toward the diffraction vector $g$ = (2$\bar{2}$0) and then tilted ≈3 degrees toward $g$ = (001). It shows clear dislocations due to the significantly reduced diffraction contrast, whereas conventional BFTEM filtering, which transmits only the beam from the perfect zone axis, produces strong background contrast from the strained interfaces, bending contours, thickness fringes, and other strain effects. Further investigation of the compositional stoichiometry of the whole structure was conducted using a STEM-energy dispersive spectrometry (EDS) chemical map in Figure S5 (Supporting Information), and the compositional line profile was overlaid as an inset on the BFTEM in Figure 2a. This confirmed that the SWIR and MWIR MQWs were grown in a multi-band structure with their respective compositions.

Cepstral 4D STEM measurements and SAD patterns were performed using a Themis 300 probe-corrected TEM (Thermo Fisher Scientific) operating at 300 kV in microprobe STEM mode, with a spot size of 6 and a semi-convergence angle of 0.6 mrad. The 4D-STEM technique involves recording local 2D diffraction patterns across a 2D array of probe positions by scanning the probe stepwise, resulting in a typical 4D dataset (2D diffraction patterns over a 2D sample array). A pixelated direct electron detector (Dectris Quadro) with a camera length of 660 mm was used to capture the diffraction patterns (256 × 256 pixels), selected to gather a sufficient number of Bragg disks for enhanced sensitivity in distortion measurement. 4D STEM maps were acquired under precession conditions (1000 Hz) using

a Nanomegas system, with a step size of 1 nm and a frame size of 200 × 200 pixels for the MQW/MQB sample, with an exposure time of 2 ms per frame. The strain distribution within the MQW/MQB was obtained from the 4D STEM data using the exit-wave powe-cepstrum transform (EWPC) following the method described by Padgett et al. (Figure S18, Supporting Information). This 4D STEM EWPC technique enables local strain measurements with sub-pm precision and sub-nm resolution. Further details are given in Note S9 (Supporting Information). SAD patterns Figure S10 (Supporting Information) were taken over MQW/MQBs of each SWIR and MWIR using a SAD aperture of 200 nm diameter.

*Artificial Neural Network Potential Calculation*: To investigate the effect of Sb incorporation into the InAs crystal structure at the atomic level, ANN-based potentials were used, which were trained on a very large database and were considered an improvement over traditional potentials in terms of generality. Using these potentials, 1000 cubic crystal structures were generated by randomly substituting Sb atoms at As atom positions, simulating a concentration of ≈10% Sb. To achieve uniform sampling of atomic structures, simulations were performed on ≈1000 independent samples, which provide representative and statistically stable results. This approach achieves a relaxation level that was seldom attainable with conventional density functional theory methods.[35]

Microscopic atomic-scale calculations were performed to investigate a realistic model incorporating doped Sb atoms, with a particular focus on changes in covalent bond lengths and angles. These calculations were compared with the reference cubic InAs crystal structure. The code developed for these calculations is available at the following website (https://github.com/inholeegithub/InAsSb_atomic_structures).

Using ANN potentials, a series of hypothetical Sb-doped cubic crystal structures were generated at the atomic level. Each structure was fully relaxed, with simultaneous optimization of crystal lattice constants and atomic positions. For these calculations, a model with 108 In atoms, 100 As atoms, and 8 Sb atoms was used to generate hypothetical crystal structures. This choice was a practical decision based on the composition of the crystal structure. A total of 1000 crystal structures were relaxed, and statistical analyses of bond lengths and angles were conducted. Initially, the cubic crystal structure of InAs was examined, and the random substitution of Sb atoms into As positions was modeled. Given the extensive range of possible crystal structures, the distributions of bond lengths were calculated, focusing on In—As and In—Sb bonds. The bond angles formed by In—As—In and In—Sb—In atomic sequences were also analyzed.

*Fabrication Feasibility Map for Monolithic Multi-Band LEDs*: Figure 5a shows the simulation-based fabrication feasibility map for the monolithic multi-band LED. The emission wavelengths of the InAsSb QWs, as a function of Sb composition and QW thickness, were modeled using the Nextnano++ simulation package. In this map, the critical thickness represents the upper limit of the dislocation-free layer. The dislocation formation region indicates where the strain energy favors dislocation formation (Note S6, Supporting Information).

## Supporting Information

Supporting Information is available from the Wiley Online Library or from the author.

## Acknowledgements

H.J.J., D.K., and P.D.N. contributed equally to this work. This research was supported by the National R&D Program through the National Research Foundation of Korea (NRF) grant funded by the Korea government (MSIT) (2022M3I8A2079227, NRF-2022M3H4A1A02076394).

## Conflict of Interest

The authors declare no conflict of interest.

## Data Availability Statement

The data that support the findings of this study are available from the corresponding author upon reasonable request.

## Keywords

infrared, light emitting diodes, metamorphic buffer layers, multi-band, quantum wells

Received: May 2, 2025
Revised: September 15, 2025
Published online:

[1] M. Sheen, Y. Ko, D.-U. Kim, J. Kim, J.-H. Byun, Y. Choi, J. Ha, K. Y. Yeon, D. Kim, J. Jung, J. Choi, R. Kim, J. Yoo, I. Kim, C. Joo, N. Hong, J. Lee, S. H. Jeon, S. H. Oh, J. Lee, N. Ahn, C. Lee, *Nature* **2022**, *608*, 56.
[2] L. Cheng, T. Jiang, Y. Cao, C. Yi, N. Wang, W. Huang, J. Wang, *Adv. Mater.* **2020**, *32*, 1904163.
[3] Z. Lin, H. Yang, S. Zhou, H. Wang, X. Hong, G. Li, *Cryst. Growth Des.* **2012**, *12*, 2836.
[4] J. Bai, Y. Cai, P. Feng, P. Fletcher, X. Zhao, C. Zhu, T. Wang, *ACS Photonics* **2020**, *7*, 411.
[5] G. Li, W. Wang, W. Yang, H. Wang, *Surf. Sci. Rep.* **2015**, *70*, 380.
[6] M. A. Khan, Y. Itokazu, N. Maeda, M. Jo, Y. Yamada, H. Hirayama, *ACS Appl. Electron. Mater.* **2020**, *2*, 1892.
[7] Y. Li, Z. Xing, Y. Zheng, X. Tang, W. Xie, X. Chen, W. Wang, G. Li, *J. Mater. Chem. C* **2020**, *8*, 883.
[8] H. N. Hussin, N. A. Talik, M. N. Abd Rahman, M. R. Mahat, P. Poopalan, A. Shuhaimi, W. H. A. Majid, *Mater. Sci. Semicond. Process* **2021**, *121*, 105431.
[9] L. Li, G. Tang, Z. Shi, H. Ding, C. Liu, D. Cheng, Q. Zhang, L. Yin, Z. Yao, L. Duan, D. Zhang, C. Wang, M. Feng, Q. Sun, Q. Wang, Y. Han, L. Wang, Y. Luo, X. Sheng, *Proc. Natl. Acad. Sci. USA* **2021**, *118*, 2023436118.
[10] L. Qi, P. Li, X. Zhang, K. M. Wong, K. M. Lau, *Light-Sci. Appl.* **2023**, *12*, 258.
[11] A. Kapoor, V. Grenier, E. Robin, C. Bougerol, G. Jacopin, B. Gayral, M. Tchernycheva, J. Eymery, C. Durand, *Adv. Photon. Res.* **2021**, *2*, 2000148.
[12] X. Zhao, K. Sun, S. Cui, B. Tang, H. Hu, S. Zhou, *Adv. Photon. Res.* **2023**, *4*, 2300061.
[13] L. Wang, X. Wang, F. Bertram, B. Sheng, Z. Hao, Y. Luo, C. Sun, B. Xiong, Y. Han, J. Wang, H. Li, G. Schmidt, P. Veit, J. Christen, X. Wang, *Adv. Opt. Mater.* **2021**, *9*, 2001400.
[14] M. Aziz, C. Xie, V. Pusino, A. Khalid, M. Steer, I. G. Thayne, D. R. S. Cumming, *Appl. Phys. Lett.* **2017**, *111*, 102102.
[15] S. Raghavan, J. M. Redwing, *J. Appl. Phys.* **2005**, *98*, 023514.
[16] I. Ahmad, M. Holtz, N. N. Faleev, H. Temkin, *J. Appl. Phys.* **2004**, *95*, 1692.
[17] A. J. O'Reilly, N. Quitoriano, *J. Cryst. Growth* **2018**, *482*, 15.
[18] K. Hjort, F. Ericson, J.-Å. Schweitz, C. Hallin, C. E. Janzén, *Thin Solid Films* **1994**, *250*, 157.
[19] N. E-Daukes, K. Kawaguchi, J. Zhang, *Cryst. Growth Des.* **2002**, *2*, 287.
[20] C. B. Carter, D. B. Williams, *Transmission Electron Microscopy: Diffraction, Imaging, and Spectrometry*, Springer, Berlin Germany **2016**.
[21] E. A. Fitzgerald, *Mater. Sci. Rep.* **1991**, *7*, 87.
[22] J. H. Lee, T. B. Holland, A. K. Mukherjee, X. Zhang, H. Wang, *Sci. Rep.* **2013**, *3*, 1061.
[23] J. Barthel, *Ultramicroscopy* **2018**, *193*, 1.

[24] B. Kim, D. Yang, W. Sohn, S. Lee, H.-H.-C. Choi, T. Jang, E. Yoon, Y. Park, H. W. Jang, *Acta Mater.* **2021**, *221*, 117423.
[25] S. Park, Y. Kim, P. D. Nguyen, J. Jeon, B. S. Chun, S. J. Lee, *Adv. Funct. Mater.* **2024**, *34*, 2309897.
[26] K. Yamaguchi, Y. Takeda, K. Kameda, K. Itagaki, *Mater. Trans. JIM.* **1994**, *35*, 596.
[27] J. C. Harmand, L. H. Li, G. Patriarche, L. Travers, *Appl. Phys. Lett.* **2004**, *84*, 3981.
[28] E. Padgett, M. E. Holtz, P. Cueva, Y.-T. Shao, E. Langenberg, D. G. Schlom, D. A. Muller, *Ultramicroscopy* **2020**, *214*, 112994.
[29] M. Hÿtch, E. Snoeck, R. Kilaas, *Ultramicroscopy* **1998**, *74*, 131.
[30] M. Nord, P. E. Vullum, I. MacLaren, T. Tybell, R. Holmestad, *Adv. Struct. Chem. Imag.* **2017**, *3*, 9.
[31] R. Guzmán, L. Maurel, E. Langenberg, A. R. Lupini, P. A. Algarabel, J. A. Pardo, C. Magén, *Nano Lett.* **2016**, *16*, 2221.
[32] S. Cai, S. Hao, Z.-Z. Luo, X. Li, I. Hadar, T. P. Bailey, X. Hu, C. Uher, Y.-Y. Hu, C. Wolverton, V. P. Dravid, M. G. Kanatzidis, *Energy Environ. Sci.* **2020**, *13*, 200.
[33] Z.-H. Ge, W.-J. Li, J. Feng, F. Zheng, C.-L. Jia, D. Wu, L. Jin, *Adv. Energy Mater.* **2022**, *12*, 2103770.
[34] M. Han, C. Wang, K. Niu, Q. Yang, C. Wang, X. Zhang, J. Dai, Y. Wang, X. Ma, J. Wang, L. Kang, W. J, J. Lin, *Nat. Commun.* **2022**, *13*, 5903.
[35] C. Chen, S. P. Ong, *Nat. Comput. Sci.* **2022**, *2*, 718.
[36] X. Li, Y. Wu, S. Zhang, B. Cai, Y. Gu, J. Song, H. Zeng, *Adv. Mater.* **2017**, *29*, 170057.